ORIGINAL PAPER

Nano-p–n junction heterostructures enhanced TiO$_2$ nanobelts biosensing electrode

Jingjie Cui · Shaowei Chen · Hong Liu · Zhen Huang

Abstract 6-Phosphate aminopurine (^{6}PA), a purine analog, is usually used in clinical anticancer treatment and biochemical research. Up to now, to the best of our knowledge, no literature about the electrochemical behaviors of ^{6}PA has been reported. In this study, nano-p–n junction heterostructures based on TiO$_2$ nanobelts were produced by the assembly of p-type semiconducting NiO nanoparticles onto the n-type surface-coarsened TiO$_2$ nanobelts. The electrochemical behaviors of ^{6}PA were investigated by different voltammetric techniques in a phosphate buffer solution of pH 7.4 using the heterostructures as the sensing electrode. Compared with single-phase TiO$_2$ nanobelt electrodes, the resulting chemically modified electrodes exhibited higher surface accumulation ability and enhanced electrocatalytic activities in the oxidation for ^{6}PA, with an irreversible oxidation peak at +0.91 V. It is proposed that the nano-p–n junction heterostructures played an important role in the enhancement of charge transport in the sensing electrodes. The results suggest that the nanoengineered TiO$_2$ nanobelts might be a promising candidate for biosensing applications of nucleic acid drugs that will be of significance to diagnostic medicine and molecular biology research.

Keywords TiO$_2$ nanobelts · NiO · Nano-p–n junction heterostructure · 6-Phosphate aminopurine · Charge transport

Introduction

For electrochemical biosensors, catalytic activity is a critical element in the selection and development of the sensing materials [1]. High-purity anatase TiO$_2$, with a high percentage of reactive {001} facets, has been found to exhibit the best catalytic activity among the four polymorphs of TiO$_2$ [2–6], which is generally desired for (bio)sensing applications. However, anatase TiO$_2$ is a semiconductor with a wide band gap (3.2 eV), and the band gap usually increases with decreasing size of the anatase domains [7], which strongly influences the charge transfer dynamics due to its increasing resistance. Thus, nanoscale engineering represents an effective route to the enhancement of the charge transport dynamics involved, such as the formation of nanoscale heterostructures with a different semiconductor [8].

Recently, we showed that TiO$_2$ nanobelts might serve as active sensing materials for electrochemical determination of purine bases and the surface-coarsened TiO$_2$ nanobelts exhibited improved sensitivity and selectivity as compared to the as-produced ones [9, 10]. Additionally, we found that interface heterostructure could enhance TiO$_2$ nanobelts' performance [11]. In the present study, we extend the investigation of coarsened TiO$_2$ nanobelts with nano-p–n junctions to electrocatalytic oxidation of 6-phosphate aminopurine (^{6}PA) by assembling NiO nanoparticles onto the TiO$_2$ nanobelts. Note that TiO$_2$ is an *n*-type semiconductor due to oxygen deficiency or excess of titanium and nickel oxide (NiO) is an antiferromagnetic p-type semiconductor with a direct forbidden band

J. Cui
College of Life Information Science & Instrument Engineering, Hangzhou Dianzi University, Hangzhou 310018, China

J. Cui (✉) · H. Liu (✉)
State Key Laboratory of Crystal Materials, Center of Bio & Micro/Nano Functional Materials, Shandong University, 27 Shandanan Road, Jinan 250100, People's Republic of China
e-mail: cuijingjie@hdu.edu.cn
e-mail: hongliu@sdu.edu.cn

S. Chen
Department of Chemistry and Biochemistry, University of California, 1156 High Street, Santa Cruz, CA 95064, USA

Z. Huang
Department of Chemistry, Georgia State University, Atlanta, GA 30302, USA

gap of 3.8 eV [12–14]. A p–n junction is thus formed when they are in intimate contact, which may be exploited for efficient charge transport.

^{6}PA, also known as adenine phosphate, is an integral part of nucleic acids. ^{6}PA participates in the synthesis of RNA and DNA in vivo. It can effectively stimulate interleukin proliferation, increasing white blood cells, and can be used in leukopenia from chemotherapy, radiation therapy, and benzene poisoning. So, ^{6}PA is usually used in clinical anticancer treatment and biochemical research. However, to the best of our knowledge, the electrochemical analysis of ^{6}PA has remained largely unexplored. Many characterization methods have been used in drug analysis, including luminescence [15], UV–vis spectroscopy [16], mass spectrometry [17], fluorescence [18], NMR [19], and electrochemical analysis [20]. Among these techniques, electrochemical detection has several advantages, such as fast response, high sensitivity, miniaturized analytical devices, in-site environmental monitoring, and analysis of very small sample volumes [21]. It is important to further develop rapid, sensitive, and simple methods for the determination of drugs.

Additionally, it should be noted that there is virtually no difference in pH between tumors and normal tissues. When eukaryotic cells clamp cytoplasmic pH at 7.0–7.4 by ion transport mechanisms and a high buffering capacity of the cytosol, the electrochemical determination of drugs must be strictly regulated in aqueous solutions within a physiological pH range from 7.0 to 7.4 [22, 23].

In this work, nano-p–n junction heterostructures based on TiO$_2$ nanobelts were produced by the assembly of p-type semiconducting NiO nanoparticles onto the n-type surface-coarsened TiO$_2$ nanobelts. The NiO nanoparticle/surface-coarsened TiO$_2$ nanobelt heterostructures (NTNs) were employed as the sensing materials that exhibited apparent electrocatalytic activity in the oxidation of ^{6}PA. Compared with the surface-coarsened TiO$_2$ nanobelts (STNs) alone, the heterostructured electrode possessed more efficient charge transfer in the oxidation of ^{6}PA. In particular, it is anticipated that the results reported in a physiological PBS of pH 7.4 herein might offer some useful information for anticancer research by electrochemical techniques, which is of particular interest for developing electrochemical sensors in physiological media.

Experimental section

Materials

Titania P-25 (TiO$_2$, ca. 75 % anatase and 25 % rutile), sodium hydroxide (NaOH), hydrochloric acid (HCl), phosphoric acid (H$_3$PO$_4$), sulfuric acid (H$_2$SO$_4$), and nickel nitrate (Ni(NO$_3$)$_2$·6H$_2$O) were purchased from China National

Medicines Corporation Ltd. ^{6}PA was obtained from Aladdin (Shanghai, China). Conductive adhesive was purchased from China Shenzhen Capiton Sci-Technology Co., Ltd. Ultrapurified (Millipore) water was used throughout this study. All reagents were of analytical grade.

Preparation of TiO$_2$ nanobelts and NiO/TiO$_2$ p–n junction heterostructures

Titanate nanobelts were synthesized by a hydrothermal process in a concentrated NaOH aqueous solution. Commercial titania powders (Degussa Co., P-25, a mixture of anatase and rutile in a ratio of 3:1) were used as the precursor. Briefly, 0.1 g of the P-25 precursor was mixed with 20 mL of a 10 M NaOH aqueous solution, followed by a hydrothermal treatment at 180 °C in a 25-mL Teflon-lined autoclave for 72 h. The treated powders were washed thoroughly with deionized water, followed by a filtration and drying process, affording sodium titanate nanobelts, which were then immersed in a 0.1 M HCl aqueous solution for 24 h and washed thoroughly with water to produce hydrogen titanate nanobelts. The hydrogen titanate nanobelts obtained were dispersed into 20 mL of 0.02 M H$_2$SO$_4$ aqueous solution with the help of magnetic stirring for half an hour. The mixed solution was then transferred into a Teflon-lined stainless steel autoclave up to 80 % of the total volume, heated at 100 °C for 12 h, and cooled to room temperature in air. The wet products were then thoroughly washed with deionized water and then dried at 70 °C to obtain surface-coarsened hydrogen titanate nanobelts (H$_2$Ti$_3$O$_7$). These nanobelts were divided into two portions. One part was thermally annealed at 600 °C for 2 h, leading to the formation of STNs. The other part was dispersed into the Ni(NO$_3$)$_2$·6H$_2$O solution (Ti and Ni in a mole ratio of 9:5) and then soaked for 5 h. Subsequently, the soaked samples were carefully collected from solution and dried in an oven at
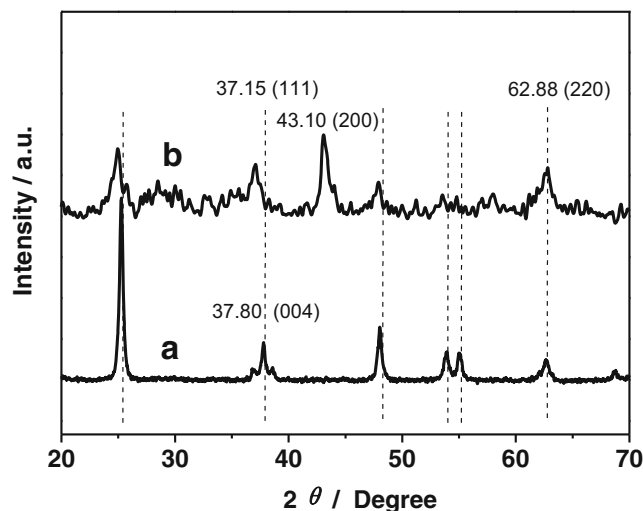
Fig. 1 X-ray diffraction (XRD) patterns of *a* surface-coarsened TiO$_2$ nanobelts and *b* nano-p–n junction heterostructure NiO/TiO$_2$ nanobelts

Fig. 2 XPS curves of nano-p–n junction heterostructure NiO/TiO$_2$ nanobelts: **a** XPS survey spectrum and high-resolution spectra of **b** Ti2p and **c** Ni2p
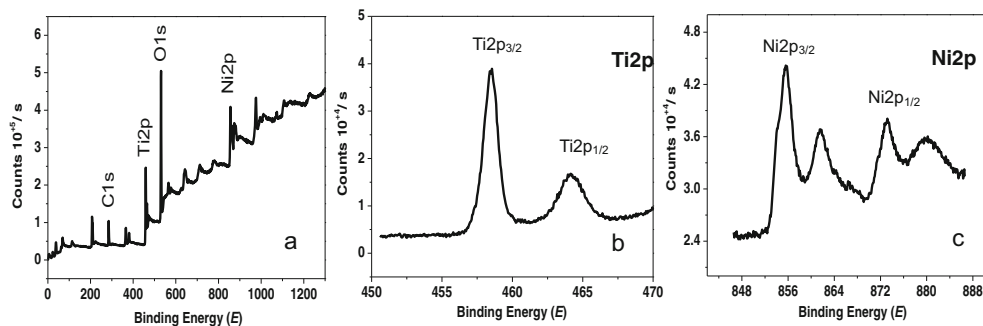
110 °C overnight. Finally, the dried samples were heat-treated at 600 °C for 2 h to obtain NiO/TiO$_2$ p–n junction heterostructures (NTNs).

Characterization

X-ray powder diffraction (XRD) patterns were obtained on a Bruker D8 Advance powder X-ray diffractometer with Cu-Ka radiation (λ=0.15406 nm). X-ray photoelectron spectroscopy (XPS) measurements were performed on a Kratos Axis Ultra DLD (delay line detector) spectrometer equipped with a monochromatic Al Ka X-ray source (1,486.6 eV). All binding energies were referenced to the C1s peak at 284.8 eV of the surface adventitious carbon. High-resolution transmission electron microscope (HRTEM) images were obtained with a JEOL JEM 2100 microscope. All experiments were performed at room temperature.

Preparation of TiO$_2$ nanobelt-modified electrodes and electrochemical studies

A glassy carbon electrode (3 mm in diameter) was polished with 0.05 μm α-Al$_2$O$_3$ suspensions until a mirror surface was obtained, and rinsed extensively with anhydrous ethanol and deionized water. The electrode was then electrochemically cleaned in 0.5 M H$_2$SO$_4$ by cycling potentials between −0.3 and +1.8 V at 100 mV s^{-1} until a steady cyclic voltammogram was produced. A conductive adhesive (CA) was drop-cast onto the cleaned glassy carbon electrode (GCE) surface, onto which 3 μL of an ethanolic suspension of TiO$_2$ nanobelts (0.5 mg mL^{-1}) was added in a dropwise fashion. After drying, the resulting electrodes were denoted as STNs/CA/GCE or NTNs/CA/GCE. Electrochemical measurements were performed in a three-electrode configuration. The TiO$_2$ nanobelt-modified electrodes prepared above were used as

Fig. 3 Microstructure of nano-p–n junction heterostructure NiO/TiO$_2$ nanobelts: **a**, **b** TEM image under different magnifications, **c** HRTEM lattice fringe images, and **d** electron diffraction images
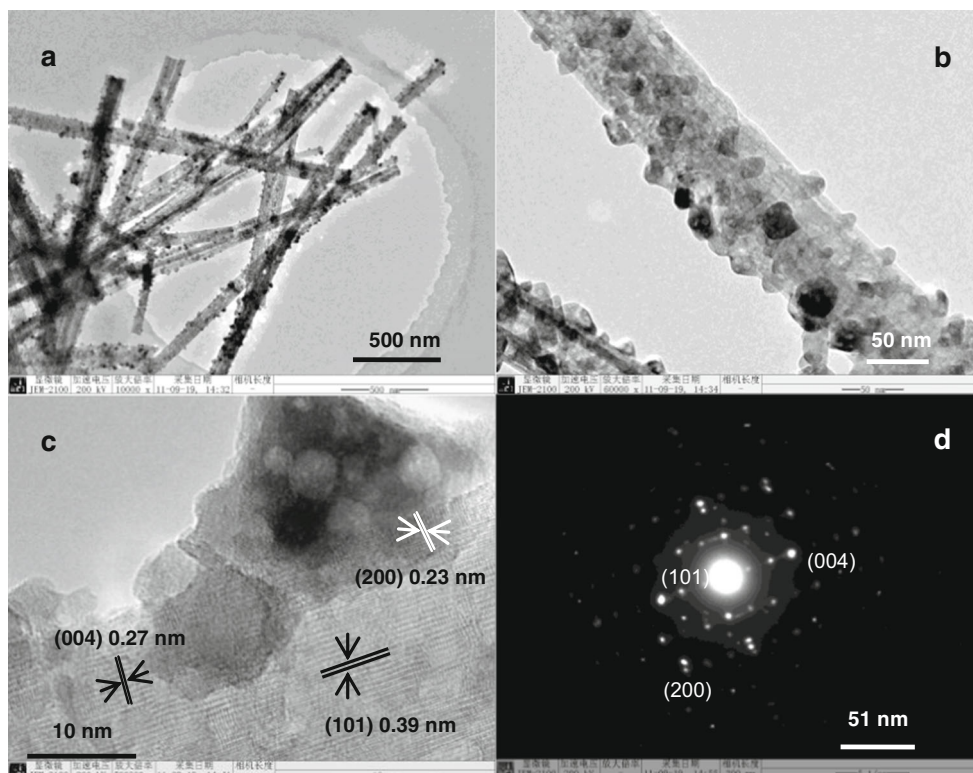
Fig. 4 Cyclic voltammograms (CV) for TiO$_2$ nanobelt electrodes in 0.1 M PBS at pH 7.4: **a** blank (CA/GCE) (*1*), surface-coarsened TiO$_2$ nanobelts (STNs/CA/GCE) (*2*), and nano-p–n junction heterostructure NiO/TiO$_2$ nanobelts (NTNs/CA/GCE) (*3*); **b** The magnified cyclic voltammogram of the partial area in **a**. Sweep rate, 100 mV s^{-1}
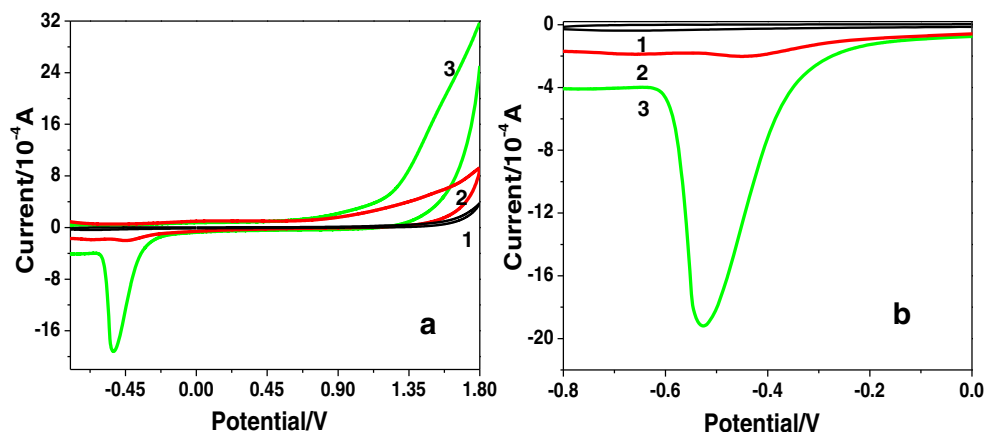
the working electrode. A Pt foil acted as the auxiliary electrode. All potentials were referred to an Ag/AgCl/KCl saturated reference electrode. All analyte solutions were prepared in 0.1 M phosphate-buffered saline (PBS) (pH 7.4). Voltammetric data were acquired with a CHI 660C electrochemical workstation.

Results and discussion

Characterization of nanobelt structure and composition

To characterize the crystal structure of the samples, XRD measurements were carried out on STNs, and NiO/TiO$_2$ p–n

junction heterostructures (NTNs). For the STNs (Fig. 1a), only anatase features were observed [9]. For the NTNs (Fig. 1b), the diffraction peaks at 37.15°, 43.10°, and 62.88° can be indexed to the (111), (200), and (220) lattice planes of cubic NiO phase (JCPDS Card 78-429), respectively. The average size of the NiO nanoparticles calculated from the width of the (200) reflection with the aid of the Scherrer equation was found to be around 20 nm. Compared to the diffraction peaks of STNs, the peaks of NTNs are broader. This is apparently due to both the smaller size of NiO and the lattice mismatch between the NiO nanoparticles and the TiO$_2$ nanobelts [24]. The latter causes additional defects in the interfacial region between the TiO$_2$ nanobelts and the NiO nanoparticles, which may enhance the surface activity of TiO$_2$ nanobelt materials.

To investigate the elemental composition of NiO/TiO$_2$ p–n junction heterostructures (NTNs), XPS was conducted. As
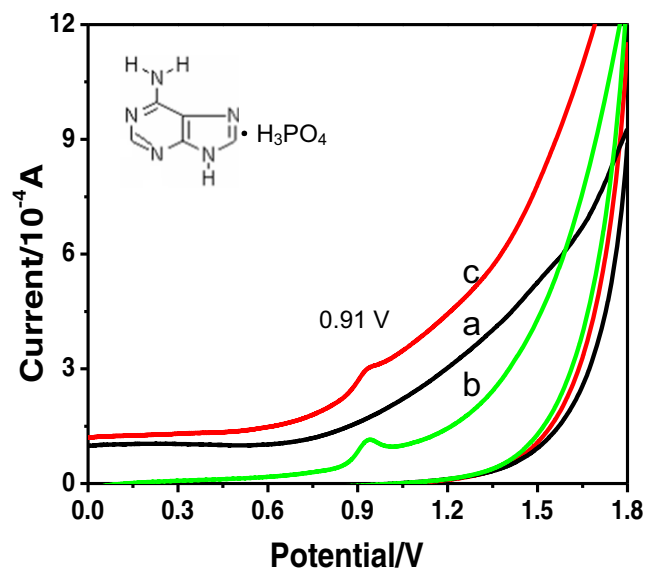
Fig. 5 Cyclic voltammograms (CV) for TiO$_2$ nanobelt-modified electrodes in 0.1 M PBS at pH 7.4 without and with 0.08 mM 6-phosphate aminopurine (^{6}PA): nano-p–n junction heterostructure NiO/TiO$_2$ nanobelt electrode in 0.1 M PBS at pH 7.4 without (*a*) and with (*b*) 0.08 mM ^{6}PA; surface-coarsened TiO$_2$ nanobelt electrode in 0.1 M PBS at pH 7.4 with ^{6}PA (*c*); molecular structure of ^{6}PA (*inset*). Sweep rate, 100 mVs^{-1}
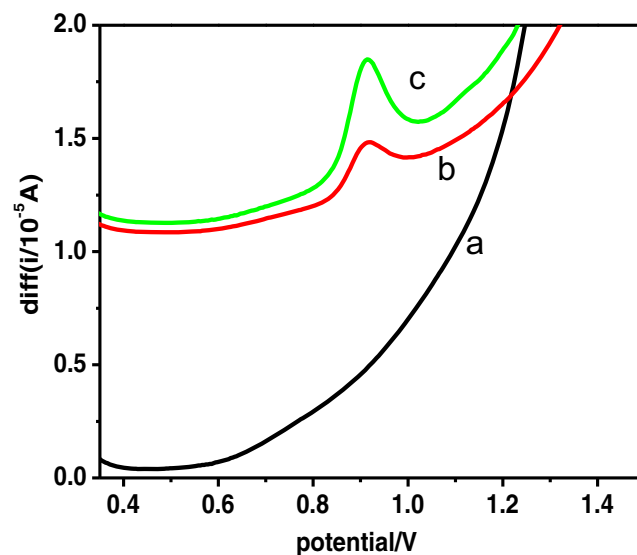
Fig. 6 Square wave voltammograms (SWV) for TiO$_2$ nanobelt-modified electrodes in 0.1 M PBS at pH 7.4 without (*a*) and with 0.08 mM 6-phosphate aminopurine (^{6}PA): surface-coarsened TiO$_2$ nanobelt electrode (*b*) and nano-p–n junction heterostructure NiO/TiO$_2$ nanobelt electrode (*c*). Sweep rate, 100 mV s^{-1}

p–n heterojunction
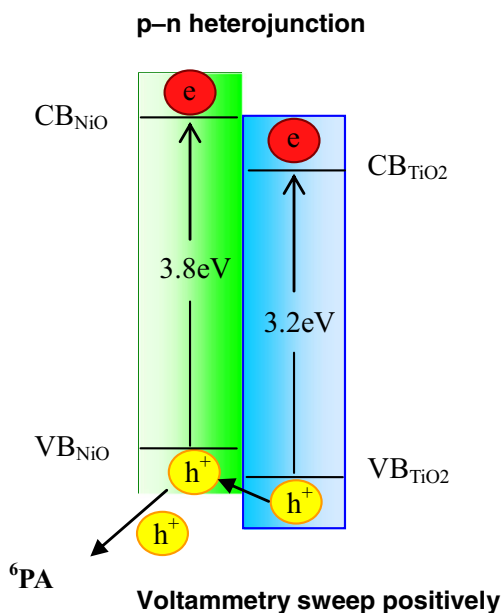
Scheme 1 The p–n junction band structure and schematic diagram of the holes driven toward solution to electrooxide ^{6}PA by the electric field (*CB* conduction band, *VB* valence band)

shown in Fig. 2a, there are Ti, Ni, C, and O elements in the XPS spectrum. The carbon element at 284.7 eV originated from the adhesive tape used in the XPS test. Panels b and c of Fig. 2 show the high-resolution XPS spectra of the Ti2p and Ni2p regions, respectively. In the high-resolution XPS spectrum of Ti2p (Fig. 2b), the binding energies of Ti 2p3/2 and 2p1/2 were centered at 458.6 and 465.2 eV, respectively, revealing that the titanium elements are in the +4 oxidation state. In the high-resolution XPS spectrum of Ni2p (Fig. 2c), the binding energies of Ni 2p3/2 and 2p1/2 were centered at 855.6 and 873.1 eV, respectively, revealing that the nickel elements are in the +2 oxidation state [25].

High-resolution transmission electron microscopy (HRTEM) examination (Fig. 3) provides more detailed information about the morphology and microstructure of the NiO/TiO$_2$ p–n junction heterostructures (NTNs). Most of the NiO nanoparticles are small nanocrystals uniformly distributed on the outermost surface of the TiO$_2$ nanobelts, resulting in a well-defined nano-p–n junction heterostructure on the TiO$_2$ nanobelt surface (Fig. 3a). The nanoparticle diameters estimated from the TEM image are about 20 nm (Fig. 3b), which is consistent with the XRD pattern calculation (Fig. 1). The lattice fringes of the NTNs can be easily seen (Fig. 3c). The distance of the aligned lattice fringe spacing was measured to be 0.39 and 0.23 nm,

which is consistent with the *d*101 spacing of anatase TiO$_2$ and the *d*200 spacing of cubic NiO. The anatase phase and cubic NiO phase are also confirmed by analyzing the electron diffraction (ED) pattern (Fig. 3d). HRTEM micrograph shows a large amount of surface defects and lattice distortion for the NTNs. This is consistent with the XRD result. It is expected that the NTNs have a high interfacial activity.

Electrochemical oxidation of 6-phosphate aminopurine

Figure 4 shows the cyclic voltammograms (CV) for the conductive adhesive (CA, curve 1), surface-coarsened TiO$_2$ nanobelts (STNs, curve 2), and NiO/TiO$_2$ p–n junction heterostructure (NTNs, curve 3) electrodes in a blank PBS (pH 7.4) supporting electrolyte. From Fig. 4a, in the potential window ranging from −0.9 to +1.8 V, no reduction peaks for the CA electrode (see curve 1) were observed, whereas an irreversible reduction peak emerged at about −0.5 V for both the STN and NTN electrodes, which may be ascribed to the electroreduction of Ti ion [26]. The fact that the voltammetric peak at NTNs/CA/GCE is much sharper and stronger than that at STNs/CA/GCE suggests that the electron transfer kinetics and electroactivity were markedly enhanced by the formation of nano-p–n junctions on the TiO$_2$ nanobelt surface with NiO nanoparticles [27].

The electrochemical activity of ^{6}PA was then investigated by the TiO$_2$ nanobelt-modified electrodes. Figure 5 shows the cyclic voltammograms of the TiO$_2$ nanobelt-modified electrodes in 0.1 M PBS (pH 7.4) in the absence and presence of 0.08 mM ^{6}PA. One can see that with the addition of 0.08 mM ^{6}PA, a new irreversible oxidation peak appeared at +0.91 V for both the NiO/TiO$_2$ p–n junction heterostructurets (NTNs/CA/GCE) and surface-coarsened TiO$_2$ nanobelt electrode (STNs/CA/GCE). The irreversible oxidation peak was not observed in a blank PBS supporting electrolyte. Different species of analytes give voltammetric signals at distinctly different potentials [28]. So, the irreversible oxidation peak at +0.91 V can be ascribed to the electrooxidation of ^{6}PA. From Fig. 5, it can be seen that the oxidation peak at NTNs/CA/GCE is sharper than that at STNs/CA/GCE, indicating faster electron transfer kinetics at the NTNs/CA/GCE electrode for ^{6}PA oxidation. Similar features were observed by square wave voltammetry (SWV) measurements.

Figure 6 shows the SWVs of varied chemically modified electrodes in the presence of 0.08 mM ^{6}PA. It can be seen that at the TiO$_2$ nanobelt-modified electrodes, the control
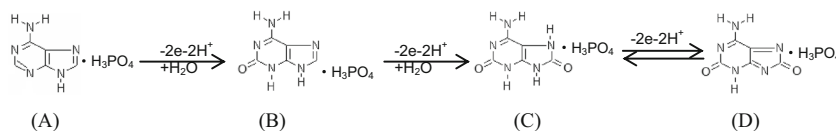
Scheme 2 The reaction mechanism for ^{6}PA: *A* 9*H*-purin-6-amine phosphate (^{6}PA), *B* 6-amino-3,9-dihydro-2*H*-purin-2-one phosphate, *C* 6-amino-7,9-dihydro-2*H*-purine-2,8(3*H*)-dione phosphate, *D* 6-amino-2*H*-purine-2,8(3*H*)-dione phosphate
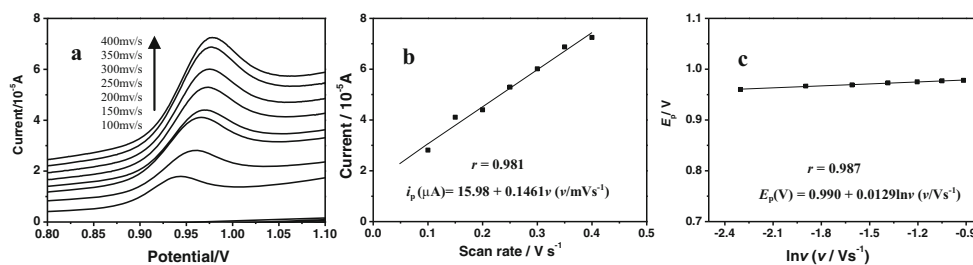
experiment in a blank PBS supporting electrolyte manifested only a featureless voltammetric profile between +0.35 and + 1.4 V (curve a). By contrast, at the TiO$_2$ nanobelt-modified (curve b, c) electrodes, an oxidation peak appeared at +0.91 V in the presence of 0.08 mM ^{6}PA. In comparison with the voltammetric responses of the STNs/CA/GCE (curves b), the peak current of the NTNs/CA/GCE (curves c) is much higher and the oxidation peak is sharper, indicating ^{6}PA possessed faster electron transfer kinetics and stronger voltammetric response at the NTNs/CA/GCE. Obviously, the nano-p–n heterostructures with enhanced (001) facets and the uniform distribution of the NiO nanoparticles play important roles in the significant improvement of the ET kinetics and the sensitivity of the TiO$_2$ nanobelt-modified electrodes [27]. For nano-p–n junction NiO–TiO$_2$ nanobelt heterostructures, an internal field is generated at the interface of the NiO–TiO$_2$ nanobelts, where the p-type NiO regions are negatively charged and the n-type TiO$_2$ regions are positively charged. Therefore, the holes flow toward the negative side, that is, the p-type NiO regions. When voltammetry sweep positively, the holes are biased toward the p-type NiO regions by the internal field. Then, the holes are driven toward solution to electrooxide ^{6}PA by the electric field (Scheme 1). The charge transport kinetics of TiO$_2$ nanobelt-modified electrodes was enhanced in this precess. It is known that holes are strong oxidants, thus facilitating the electrooxidation of ^{6}PA.

Electrochemical oxidation mechanism and kinetics of 6-phosphate aminopurine at the TiO$_2$ nanobelt electrodes

^{6}PA, also known as adenine phosphate, contains one-molecular adenine and one-molecular phosphate. The chemical structure of ^{6}PA is shown in the Fig. 5 inset. The

phosphate and amino moieties are good anchoring groups to immobilize ^{6}PA onto the p–n junction heterostructuret oxide surface. Obviously, its electroactivity arises from its adenine structure [9]. The relevant mechanism in electrooxidation of ^{6}PA may be proposed as follows (Scheme 2).

Additionally, the electrochemical kinetics of ^{6}PA at the TiO$_2$ nanobelt (STNs or NTNs) modified electrode was then examined by cyclic voltammetric measurements at different potential sweep rates (Figs. 7 and 8). It can be seen that the oxidation peak currents of ^{6}PA increase linearly with the potential scan rate at the modified electrode. The linear regression equations and correlation coefficient can be seen in Figs. 7b and 8b. These phenomena indicated that the process of electrode was controlled by surface adsorption.

For an irreversible surface process, where adsorbed species are oxidized, the relationship between peak current (i_p) and surface coverage (Γ) is [29]

$$i_p = n(1-\alpha)n_\alpha AF^2 v\Gamma / 2.718RT \tag{1}$$

where v is the scan rate, R the gas constant (8.314 J mol^{-1} K^{-1}), T the absolute temperature (T=298 K), F the Faraday constant (96,485 C mol^{-1}), A the geometrical area of the working electrode (A=0.07 cm^2), n the total number of electrons involved in the oxidation of ^{6}PA (^{6}PA consists of one adenine and one phosphate; here, n may be thought as 6 due to its electroactivity from the adenine group.) [30, 31], n_α the number of electrons involved in the rate-determining step, and α the electron transfer coefficient, which can be determined by the linear dependence of peak potential E_P with the logarithm of the potential scan rate v (Figs. 7c and 8c) [29, 32], according to

$$E_{pa} = \text{const.} + [0.02569/(1-\alpha)n_\alpha]\ln v \ (298 \ K) \tag{2}$$
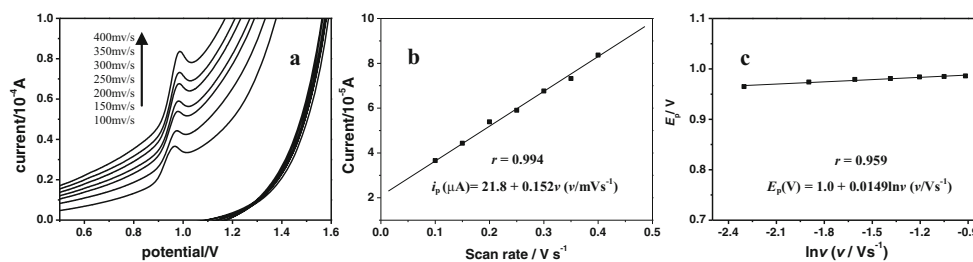
In the potential range examined, the plots of E_p vs $\ln\nu$ were linear. The equation of the straight lines is shown in Figs. 7c and 8c. The ^{6}PA at the STNs/CA/GCE and the NTNs/CA/GCE, $(1-\alpha)n_\alpha$, were estimated as 1.9915 and 1.7242, respectively. Thus, if a flat surface is assumed, the average surface concentration (I) of ^{6}PA on the surfaces of the STNs/CA/GCE and the NTNs/CA/GCE are estimated to be about 1.934×10^{-6} and 2.587×10^{-6} mol/m^2, respectively. These results indicate that the NiO/TiO$_2$ p–n junction heterostructuret nanobelts (NTNs) have higher surface accumulation ability for all detected species because the heterostructures may increase surface adsorption active sites.

Conclusions

Nano-p–n junction heterostructures based on TiO$_2$ nanobelts (NTNs) have been produced by assembling p-type semiconducting NiO nanoparticles onto the n-type surface-coarsened TiO$_2$ nanobelts through a chemical deposition/decomposition process. The electrochemical results indicated that the nanobelt-functionalized electrodes had a markedly enhanced electrocatalytic activity and sensitivity in the oxidation of ^{6}PA. The enhanced performance is most likely due to the nano-p–n junctions and the uniform distribution of the NiO nanoparticles on the TiO$_2$ nanobelt surface that effectively improved charge transport at the interface. These results suggest that nano-p–n junction heterostructure NiO/TiO$_2$ nanobelts may serve as promising active materials in the electrochemical oxidation of ^{6}PA, which will be of significance to modern biochemical and biomedical research by the electrochemical technology.

References

1. Li XC, He GH, Han Y, Xue Q, Wu XM, Yang SR (2012) J Colloid Interface Sci 387:39–46
2. Zhang J, Li LP, Li GS (2012) Phys Chem Chem Phys 14:11167–11177
3. Banfield JF, Veblen DR (1992) Am Mineral 77:545–557
4. Yang HG, Sun CH, Qiao SZ, Zou J, Liu G, Smith SC, Cheng HM, Lu GQ (2008) Nature 453:638–642
5. Wang W, Ni YR, Lu CH, Xu ZZ (2012) RSC Adv 2:8286–8288
6. Barbora L, Marketa Z, Ladislav K, Alison C, Paul L, Zhang W, Liu B, Pavel K, Elham G, Jacques EM, Michael G (2012) J Solid State Electrochem 16:2993–3001
7. Chen XB, Mao SS (2007) Chem Rev 107:2891–2959
8. Wu R, Chen XH, Hu JQ (2012) J Solid State Electrochem 16:1975–1982
9. Cui JJ, Sun DH, Zhou WJ, Liu H, Hu PG, Ren N, Qin HM, Huang Z, Lin JJ, Ma HY (2011) Phys Chem Chem Phys 13:9232–9237
10. Cui JJ, Sun DH, Chen SW, Zhou WJ, Hu PG, Liu H, Huang Z (2011) J Mater Chem 21:10633–10636
11. Zhou WJ, Gai LG, Hu PG, Cui JJ, Liu XY, Wang DZ, Li GH, Jiang HD, Liu D, Liu H, Wang JY (2011) CrystEngComm 13:6643–6649
12. Lee CY, Chiang CM, Wang YH, Mac RH (2007) Sensors Actuators B 122:503–510
13. Hotovy I, Rehacek V, Siciliano P, Caponec S, Spiess L (2002) Thin Solid Films 418:9–15
14. Mattei G, Mazzoldi P, Post ML, Buso D, Guglielmi M, Martucci A (2007) Adv Mater 19:561–564
15. Li PP, Liu SP, Yan SG, Fan XQ, He YQ (2011) Colloids Surf A 392:7–15
16. Park EK, Lee SB, Lee YM (2005) Biomaterials 26:1053–1061
17. Hartinger CG, Ang WH, Casini A, Messori L, Keppler BK, Dyson PJ (2007) J Anal At Spectrom 22:960–967
18. Win KY, Feng SS (2005) Biomaterials 26:2713–2722
19. Iwamoto M, Mukundan S Jr, Marzilli LG (1994) J Am Chem Soc 116:6238–6244
20. El-Said WA, Yea CH, Kim H, Oh BK, Choia JW (2009) Biosens Bioelectron 24:1259–1265
21. Wang J (2002) Anal Chim Acta 469:63–71
22. Madshus IH (1988) Biochem J 250:1–8
23. Povsic TJ, Dervan PB (1989) J Am Chem Soc 111:3059–3061
24. Zhou XD, Huebner W (2001) Appl Phys Lett 79:3512–3514
25. Chen SF, Zhang SJ, Liu W, Zhao W (2008) J Hazard Mater 155:320–326
26. Tomčík P, Jenčušová P, Krajčíková M, Bustin D, Manová A, Čakrt M (2006) J Electroanal Chem 593:167–171
27. Cui JJ, Ge YK, Chen SW, Liu H, Huang Z, Jiang HD, Chen J (2013) J Mater Chem B 1:2072–2077
28. Nowicka AM, Zabost E, Donten M, Mazerska Z, Stojek Z (2007) Anal Bioanal Chem 389:1931–1940
29. Bard AJ, Faulkner LR (2001) Electrochemical methods: fundamentals and applications. Wiley, New York
30. de los Santos-Alvarez N, de los Santos-Alvarez P, Lobo-Castanon MJ, Lopez R, Miranda-Ordieres AJ, Tunon-Blanco P (2007) Electrochem Commun 9:1862–1866
31. Wang ZH, Xiao SF, Chen Y (2006) J Electroanal Chem 589:237–242
32. Laviron E (1974) J Electroanal Chem 52:355–393